

## A comparative research on bobbin tool and conventional friction stir welding of Al-Mg-Si alloy plates

C. Yang<sup>a,b</sup>, D.R. Ni<sup>a,\*</sup>, P. Xue<sup>a</sup>, B.L. Xiao<sup>a</sup>, W. Wang<sup>c</sup>, K.S. Wang<sup>c</sup>, Z.Y. Ma<sup>a,\*</sup>

<sup>a</sup> Shenyang National Laboratory for Materials Science, Institute of Metal Research, Chinese Academy of Sciences, 72 Wenhua Road, Shenyang 110016, China

<sup>b</sup> School of Materials Science and Engineering, University of Science and Technology of China, 72 Wenhua Road, Shenyang 110016, China

<sup>c</sup> School of Metallurgical Engineering, Xi'an University of Architecture and Technology, Xi'an 710055, China



### ARTICLE INFO

#### Keywords:

Aluminium alloy  
Friction stir welding  
Bobbin tool  
Microstructure  
Mechanical properties

### ABSTRACT

In our work, Al-Mg-Si (6061Al-T4) plates of 6 mm thickness were subjected to bobbin tool friction stir welding (BT-FSW) and conventional friction stir welding (C-FSW) for comparison. How the welding process affects the microstructure and mechanical properties was investigated at various rotation rates and welding speeds. The results showed that butt FSW joints with high quality could be produced at the selected parameters. The joint strength rose with enhanced welding speed and was nearly independent of the rotation rate in both the welding processes. The strength of the joints produced with BT-FSW reached the same level as that of the C-FSW. The maximum joint strength of 229 MPa was 93% of the base material (BM), which is superior to the reported results of 60–80% for the T4 condition. The fracture position of most of the joints was in the heat-affected zone (HAZ), which is the lowest hardness zone.

### 1. Introduction

6061 Al alloy, which is typical of the 6xxx (Al-Mg-Si) series, has outstanding mechanical properties, good corrosion resistance and weldability, which renders it useful in various applications in many fields such as aerospace, automotive, shipbuilding, and other industries [1,2]. Welding, as an essential joining method, furthers its applications in many industrial fields. However, fusion welding can cause many welding defects and disadvantages during the welding of precipitation-strengthened aluminium alloys.

Friction stir welding (FSW) [3], which is a solid-state joining process, has been invented to join aluminium alloys while overcoming the problems faced in fusion welding. FSW has great advantages over fusion welding in joining light alloys such as magnesium and aluminium alloys [3,4]. Besides, high quality joints of aluminium matrix composites [5–7] and dissimilar alloys [8–10] can be acquired by FSW or its derivative process [11,12]. However, conventional friction stir welding (C-FSW) has a high demand for clamping and also a backing anvil; besides, there is a risk of root defects, like kissing bonds and lack of penetration, and non-uniform heat input can occur in the process [13–15].

Bobbin tool friction stir welding (BT-FSW), also called self-support friction stir welding (SS-FSW) [16,17], has remarkable potential to overcome the above problems encountered in the C-FSW process. The so-called bobbin tool consists of two shoulders, namely the upper shoulder and the lower shoulder, connected by a pin between them. The process is performed with the two shoulders in contact with the surface of the workpiece and it enables a balanced axial force and uniform temperature gradient through the thickness direction of the weld. Additionally, the two-shoulder feature enables it to join hollow extrusion profiles, expanding its applications greatly [4,16,17].

To date, there have been systemic reports on FSW of 6061Al [18–24], but studies on BT-FSW of 6xxx series aluminium alloys [25–28] are still insufficient, and many less than C-FSW. As mentioned above, root flaws, especially kissing bonds and a lack of penetration, are inclined to be generated for medium thick plate in the C-FSW process when the parameters are unsuitable [13,29–31]. BT-FSW has the potential to avoid these root defects due to its unique features.

The limited process window and wider softened area of the joint are the main problems currently faced in BT-FSW. Usually, the as-welded joints produced by BT-FSW have lower strength than those of C-FSW. Lafly et al. [32] reported that the BT-FSW joint strength was lower than

*Abbreviations:* FSW, friction stir welding; BT-FSW, bobbin tool friction stir welding; C-FSW, conventional friction stir welding; NZ, nugget zone; TMAZ, thermo-mechanically affected zone; HAZ, heat-affected zone; BM, base material; JLR, joint line remnants; LHZ, lowest hardness zone; UTS, ultra tensile strength; EBSD, electron backscattered diffraction; TEM, transmission electron microscopy; SEM, scanning electron microscopy; T4, natural aging after solid solution heat-treatment

\* Corresponding authors.

E-mail addresses: [drni@imr.ac.cn](mailto:drni@imr.ac.cn) (D.R. Ni), [zyrna@imr.ac.cn](mailto:zyrna@imr.ac.cn) (Z.Y. Ma).

<https://doi.org/10.1016/j.matchar.2018.08.027>

Received 5 June 2018; Received in revised form 22 July 2018; Accepted 17 August 2018

Available online 18 August 2018

1044-5803/© 2018 Elsevier Inc. All rights reserved.

that of a C-FSW joint for 6056 alloy. Zhang et al. [33] conducted the BT-FSW/C-FSW of AA2219-T4 alloy and also acquired lower joint strengths by BT-FSW compared with C-FSW. Esmaily [25] compared the microstructure and properties of the BT-FSW and C-FSW processes for 6005-T6 plates of 10 mm thickness, and although a high strength joint by BT-FSW was acquired, it was conducted under only one parameter combination (900–1200), and the process window was very limited.

The present work is aimed at illuminating the weldability of 6061-T4 Al alloy subjected to the BT-/C-FSW processes, and identifying the different effects of the two welding processes on the evolution of microstructure and its relationship with the mechanical properties of the welds.

## 2. Experiment

The base material (BM) for butt welding was 6.35 mm thick 6061Al-T4 plates (T4 treatment: natural aging after solid solution heat-treatment) with dimensions of 320 mm × 80 mm. The chemical composition of the BM is 1.0 Mg, 0.6 Si, 0.25 Zn, 0.25 Cu, 0.7 Fe, 0.15 Mn, 0.08 Cr, 0.15 Ti, and balance Al (wt%).

The welding processes (BT-FSW and C-FSW) were both carried out using a numerically controlled FSW machine (FSW-5LM-020) and the welding was conducted in a parallel direction to the rolling direction of the BM. The tilt angle of the tool was 2.75° and 0° in the C-FSW and BT-FSW processes, respectively. The bobbin tool used in the experiment consisted of symmetrical upper and lower shoulders with a scrolled groove feature 22 mm in diameter, and was connected by a cylindrical pin with a mixed thread 8 mm in diameter and 6 mm in length. The C-FSW tool consisted of a 22 mm diameter concave shoulder and a cylindrical right-threaded pin 8 mm in diameter and 6 mm in length. The figures of the welding tools were presented in Fig. 1. To demonstrate the effect of the rotation rate, the welding speed was kept constant at 100 mm/min while the plates were subjected to BT-FSW and C-FSW processes at three rotation rates of 300, 400 and 600 rpm for comparison. A constant rotation rate was then maintained at 600 rpm while four welding speeds of 50, 100, 150 and 300 mm/min were conducted to demonstrate the effect of the traversing speed. The variable rotation rate groups of the corresponding joints were respectively defined as BT-300-100, BT-400-100, BT-600-100, C-300-100, C-400-100, and C-600-100; the variable traversing parameters of the corresponding joints were defined as BT-600-50, BT-600-150, BT-600-300, C-600-50, C-600-150 and C-600-300.

Microstructural observations were conducted using optical microscopy (OM), scanning electron microscopy (SEM), transmission electron microscopy (TEM), and electron backscattered diffraction (EBSD). OM

observation was carried out with the samples prepared by grinding, polishing, and etching with Keller's reagent (NH<sub>3</sub>: HCl: HF: H<sub>2</sub>O = 2.5: 1.5: 1: 95 vol%). The fracture morphology of failed tensile samples was observed by SEM after tensile tests. Twin-jet electro-polishing was used to prepare samples for TEM observation with a 30% nitric acid and 70% methanol solution (temperature: −30 °C; voltage: 15 V). Grain structure and mean size were ascertained by EBSD. Samples for EBSD were prepared by grinding and mechanical polishing, followed by electro-polishing in a solution of 10% perchloric acid and 90% alcohol solution at −25 °C and 15 V for 1 min.

An auto testing machine (Leco, LM-247AT) was used for hardness measurement on the cross-section along the centre line across the weld under a load of 300 g, holding for 15 s. Tensile specimens with a gauge 50 mm in length and 10 mm in width were machined perpendicular to the welding direction. Room-temperature tensile tests were conducted at a constant strain rate of  $1 \times 10^{-3} \text{ s}^{-1}$ , and each parameter was tested at least three times for accurate results. All the FSW samples were kept 1 month before examinations of the microstructure and mechanical properties after FSW.

## 3. Results and Discussion

### 3.1. Microstructure Evolution

Cross-sectional microstructures of the joints at various rotation rates are presented in Fig. 2. Fig. 2a–c shows the BT-FSW joints and Fig. 2d–f the C-FSW joints. Defect-free joints were generated during welding, and all the BT/C-FSW joints exhibited four microstructural zones: nugget zone (NZ), thermo-mechanically affected zone (TMAZ), heat-affected zone (HAZ), and base material (BM). Unlike the C-FSW joints, the NZ in BT-FSW joints has an hour-glass shape. This is attributed to the contact and friction heat produced from both the upper and lower shoulders. An apparently sharp boundary between the NZ and TMAZ could be found on the advancing side (AS) in both the BT/C-FSW joints. This phenomenon is attributed to the intense plastic deformation and material flow during welding [3,25]. It is noticed that zig-zag lines (“S” lines) or joint line remnants (JLR) are quite evident in the centre of the joints, especially for BT-FSW joints. For the C-FSW joints, they are inclined to the AS.

The cross-sectional microstructures of the BT-FSW and C-FSW joints at various welding speeds are presented in Fig. 3. Fig. 3a–d shows the changing tendency when increasing the welding speed of the BT-FSW joints, and Fig. 3e–h shows the C-FSW joints. JLRs can also be observed in the centre of the weld, and, with increase of the welding speed, the profiles of the NZ and JLRs become indistinct at high welding speed

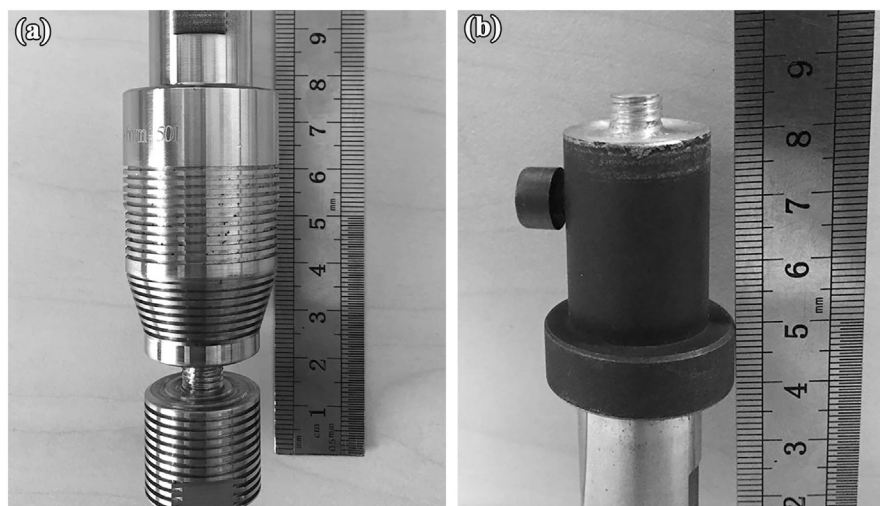


Fig. 1. Picture of welding tools: (a) bobbin tool; (b) conventional tool.

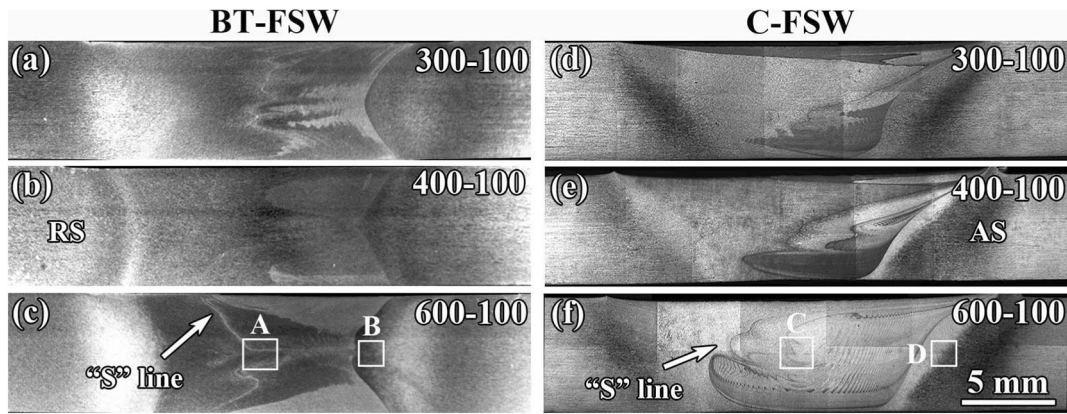


Fig. 2. BT-FSW and C-FSW joints of 6061Al-T4 plates produced at various rotation rates (RS: retreating side; AS: advancing side).

(300 mm/min). For C-FSW joints, the JLRs are off to the AS and not as evident as in the BT-FSW joints. What should be noted is that a defect-like small hole appears at the NZ/TMAZ boundary at the AS of the BT-600-300 joint, but it has no destructive effect on the tensile properties, as will be shown below. This phenomenon demonstrates that BT-FSW has a narrow welding parameter window.

Fig. 4a shows the EBSD microstructure of the BM, which is characterized by elongated grain structures due to the rolling process, and the mean width and length of the grains are  $\sim 25 \mu\text{m}$  and  $\sim 90 \mu\text{m}$ , respectively. Fig. 4b shows the TEM image in the bright field pattern of the BM, where it can be seen that there are only some dislocations in the BM, without precipitates being observed, and this is attributed to the T4 condition. Magnesium and silicon are the major alloying elements in 6000 series aluminium alloys. During natural aging (NA) after solid solution treatment, nano-scale clusters are formed, which are believed to be Si-rich clusters or co-clusters of Mg + Si and are regarded as precursors of  $\beta''$  in consequent heat-treatment [34,35]. This is quite different from the 6061Al under the T6 condition, which is strengthened by precipitated  $\beta$  ( $\text{Mg}_2\text{Si}$ ) phase [36].

Fig. 5 shows the EBSD maps of NZs and TMAZs of typical joints BT-600-100 and C-600-100. The selected zones are marked with the white line boxes in Fig. 2. All the NZs are characterized by equiaxed recrystallized grains with a mean grain size of  $13 \mu\text{m}$  for BT-600-100 and  $12 \mu\text{m}$  for C-600-100 (Fig. 5a and c). Unlike the NZ, deformed coarse and fine mixed grain structure was observed in the TMAZs due to the incomplete recrystallization. It is mainly insufficient deformation strain

that induces this phenomenon despite the high-temperature exposure. The TMAZ in BT-FSW underwent more intense plastic deformation than that in C-FSW, as a result of a higher fraction of fine grains can be seen in the TMAZ of joint BT-600-100 compared with joint C-600-100 (Fig. 5b and d).

To illuminate the evolution of precipitates in the HAZs (fracture position), two typical parameters (BT-600-100 and C-600-100) were selected to conduct a TEM examination of the HAZs. Fig. 6 shows the bright-field TEM images of joints BT-600-100 and C-600-100. An incident direction parallel to the  $\langle 100 \rangle$  zone axis of the BM of the electron beam was selected in each micrograph.

The BT-600-100 joint was characterized by a high density of coarsening rod-shaped precipitates about 200 nm in length (Fig. 6a). The C-600-100 joint featured relatively fine rod-shaped precipitates (Fig. 6b).

The precipitation sequence of Al-Mg-Si series alloys during aging is documented as below: supersaturated solid solution  $\rightarrow$  needle-shaped precipitates  $\rightarrow \beta'$  precipitate  $\rightarrow \beta\text{-Mg}_2\text{Si}$  [37–40], which has been widely reported. The  $\beta'$  phase is characterized by coarse rods about 50 to 700 nm in length [38,39]. This proves that the precipitates of 200 nm length in the HAZs of the joints in our study are  $\beta'$  phases, and these could not strengthen the alloy effectively.

The precipitates are dominated by the thermal history in the HAZ during welding. The occurrence of precipitation from matrix in the HAZ was attributed to the thermal cycles it underwent during welding. Liu et al. [37] and Sato's et al. [41] investigated the distribution of temperature in conventional FSW of 6000 series Al alloys, and their results

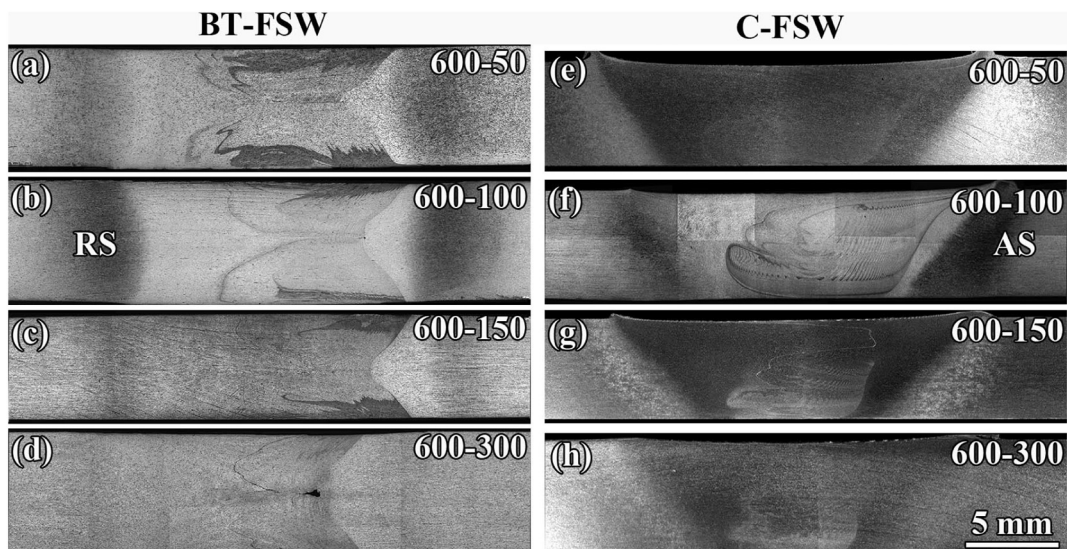


Fig. 3. BT-FSW and C-FSW joints of 6061Al-T4 plates produced at various welding speeds (RS: retreating side; AS: advancing side).

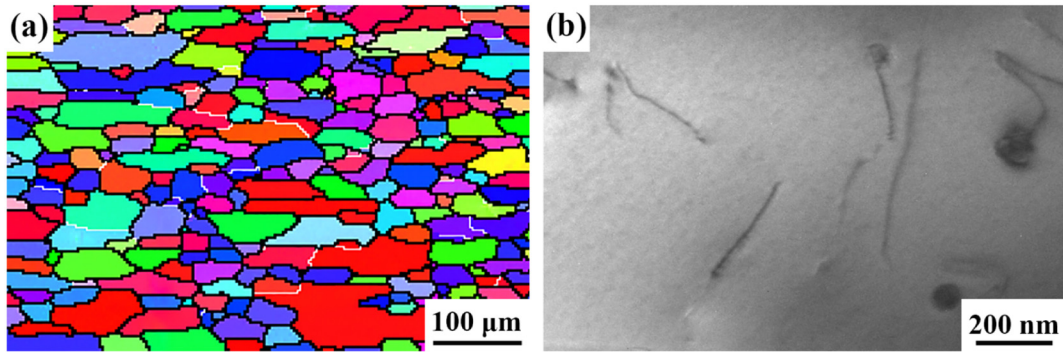


Fig. 4. (a) EBSD map and (b) bright field TEM image of 6061Al-T4 plate base material.

showed that the peak temperature in HAZ was measured to be  $\sim 370$  °C, and the peak temperature in NZ could surpass 402 °C.

Liu et al. [37] have proposed a model called the Heat Source Zone–Isothermal Dissolution Layer in FSW of 6061Al alloy. They demonstrated that thermal cycles from the NZ, which was defined as the heat source, were exerted on the HAZ and the peak temperature in the HAZ was independent of the welding parameters and tool dimensions. When the welding speed was constant, the rotation rate just induced the position of the HAZ (LHZ) to move outward or inward, while the peak temperature in the HAZ was approximately the same. When the welding speed was increased, it led to a decreased dissolution time, i.e., a faster heating and cooling rate. The HAZs were defined as an Isothermal Dissolution Layer due to the nearly constant peak temperature. Therefore, the LHZ was located consistently in the HAZ.

However, in our study, the peak temperature during thermal cycles for BT-FSW was higher in the heat source (NZ) than that of C-FSW at a certain rotation rate (600 rpm), which would result in a slower cooling rate in the HAZ after welding. The slower cooling rate allowed more time for precipitation and coarsening of  $\beta'$  in the HAZ of the BT-600-100 joint compared with the C-600-100 joint, as presented in Fig. 6a and b.

### 3.2. Microhardness

The Vickers' hardness profiles along the centre line of the thickness direction on the cross-section surface of the joints are presented in Fig. 7. The hardness curves of joints produced at different rotation rates are presented in Fig. 7a and b. The curves delivered several messages. First, the curves all presented a “W” shape. Second, under the same process, it was apparently shown that the highest hardness was located in the BM and the lowest hardness zone (LHZ) was located in the HAZ, then it recovered in the NZ to almost the same level as the BM. The position of the LHZ moved outward and the hardness value in the NZ enhanced slightly when increasing the rotation rate. Finally, it was notable that the lowest hardness and the hardness in the NZ of BT-FSW joints achieved nearly the same level as in the C-FSW joints.

The changing tendency of the hardness across the joints under different welding speeds is shown in Fig. 7c and d. The curves all presented a “W” shape, except for the high welding speed joints (BT-600-300 and C-600-300). For each given process, the hardness values achieved almost the same level in the NZs at different welding speeds. With increase of the welding speed, the value in the LHZ was enhanced. For BT-FSW, the value in the LHZ was  $\sim 50$  at the welding speed of 50 mm/min and rose to  $\sim 65$  at 300 mm/min. The tendency was the

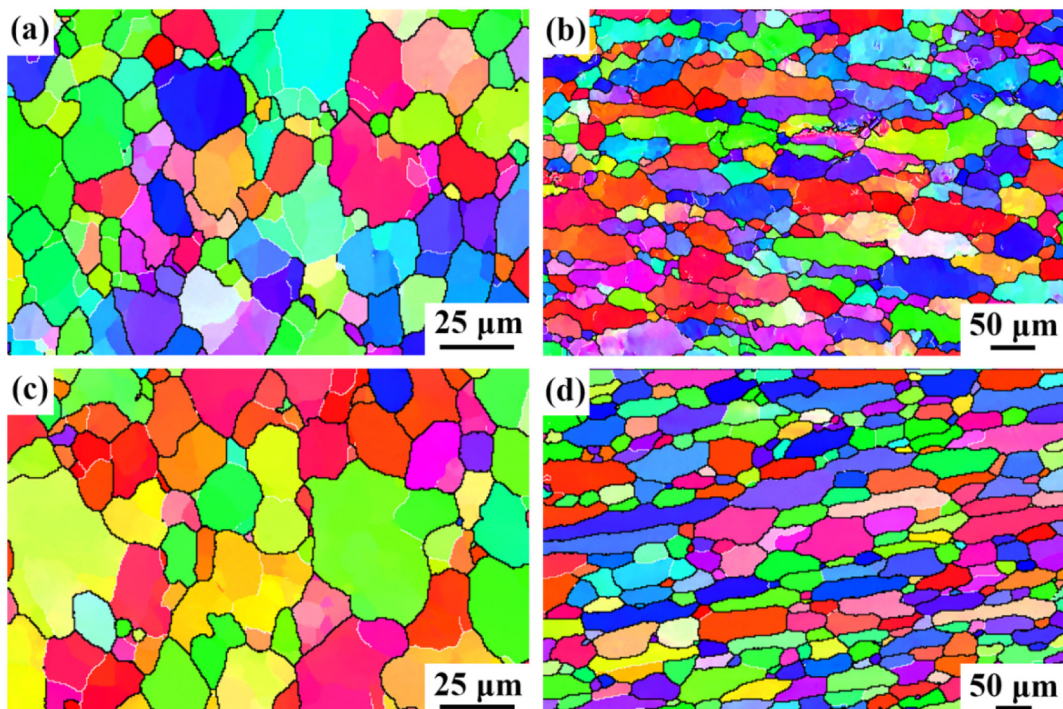


Fig. 5. EBSD maps of 6061Al-T4 joints: (a) NZ and (b) TMAZ of BT-600-100, (c) NZ and (d) TMAZ of C-600-100.

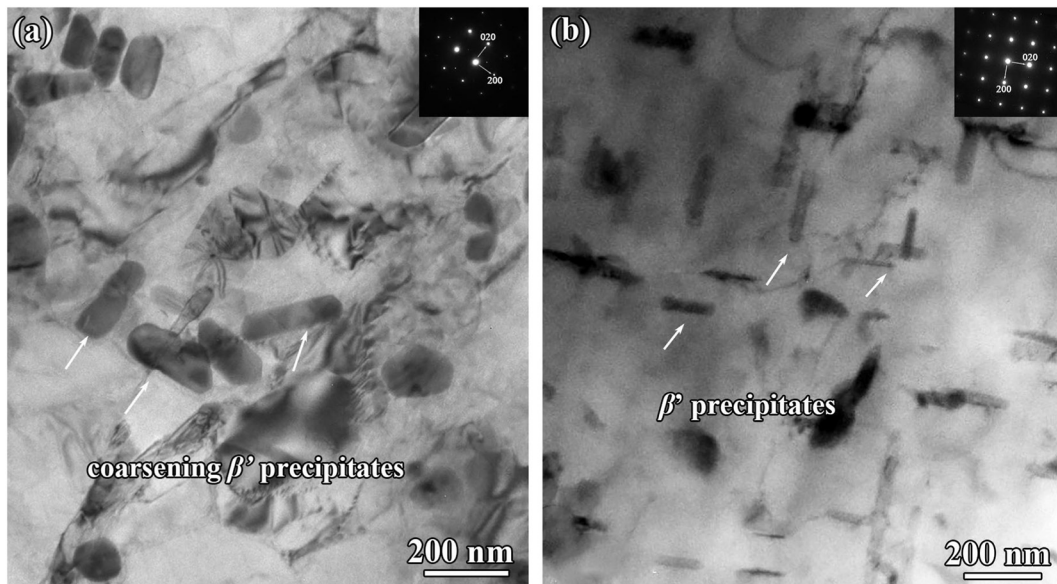


Fig. 6. Bright-field TEM micrographs of HAZ in: (a) BT-600-100 joint, (b) C-600-100 joint.

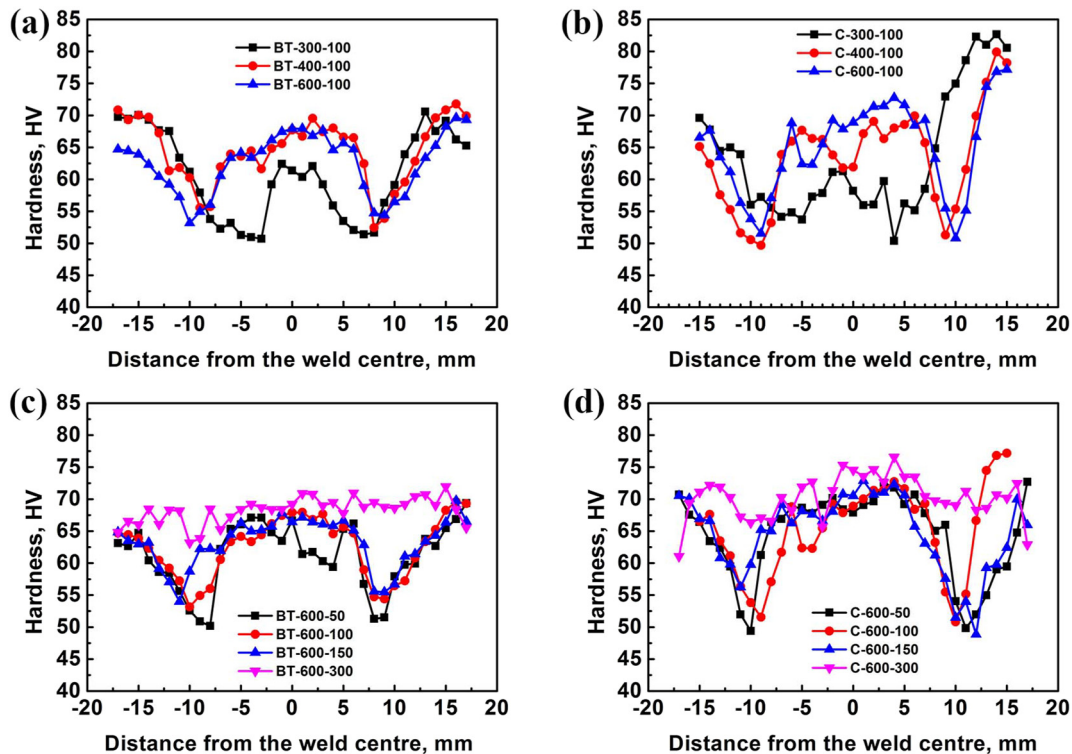


Fig. 7. Microhardness profiles of 6061Al-T4: (a) BT-FSW and (b) C-FSW joints at different rotation rates, (c) BT-FSW and (d) C-FSW joints at different welding speeds (AS on right side; RS on left side in a–d).

same for the C-FSW joints, but not as evident as for the BT-FSW joints.

The HAZ underwent intense thermal cycles during the welding process, which led to the precipitation and coarsening of the precipitates in this zone. The coarsening precipitates resulted in the lowest hardness value in the HAZ. The hardness values in the LHZ were independent of the rotation rate (Fig. 7a and b) and increased with increase of the welding speed (Fig. 7c and d). This is because the rotation rates do not affect the peak temperature and heating and cooling rates in the LHZ, but just change its position. Although the increasing welding speed does not change the peak temperature in the LHZ either, it causes faster heating and cooling rates in the LHZ, leaving a shorter

time for the precipitates to coarsen. Therefore less coarsening of precipitates at high welding speed brings a rise in hardness in the LHZs [37]. The hardness in the NZ recovered to the level of the BM, and it has been reported that this recovery can be attributed to the mixed effects of fine recrystallized grains, precipitates evolution, and dislocation in the NZ for precipitation-hardened aluminium alloys [3,42].

### 3.3. Tensile Properties

The rotation rate–tensile strength histogram is presented in Fig. 8a. The ultimate tensile strength (UTS) of the joints was almost

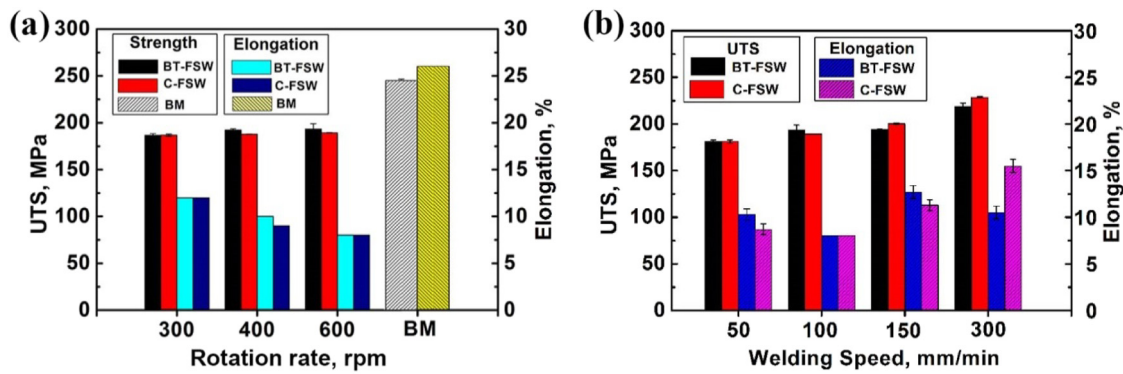


Fig. 8. Tensile strength histograms of 6061Al-T4: (a) BM and FSW joints at different rotation rates; (b) joints at different welding speeds.

independent of the rotation rates, with only a small fluctuation for both the BT-FSW and C-FSW joints. The strength of C-FSW joints is between 186–189 MPa, and the range is 185–199 MPa for BT-FSW joints. The maximum tensile strength (199 MPa) was obtained with the parameter BT-600-100, which was 81% of that of the BM. We can conclude that, compared to the C-FSW joints, the BT-FSW joints exhibited an equivalent or slightly enhanced strength value at each selected rotation rate.

The UTS versus welding speed histogram in Fig. 8b shows that the UTS of the joints rose with increased welding speed under the same process, which is a good match with the hardness profile. Meanwhile, there were no distinct differences between the joints produced by the two processes respectively at the same welding speed. The range of the UTS of BT-FSW joints at different welding speeds was 181–222 MPa, and for C-FSW joints it was 181–229 MPa. The maximum UTS (229 MPa) was achieved with the C-600-300 parameter, which was 93% of BM.

Lafly [32] et al. reported that for a 6056Al alloy with different heat-treatment conditions (T4, T6, T78) the BT-FSW joints usually exhibited a tendency of lower strength than the C-FSW joints. The strength efficiency of as-welded joints at each heat-treatment condition was about 89% for the conventional process and 83% for the unconventional process (bobbin tool welding). The author attributed this to the high heat input with the function of the two shoulders, and more heat input led to a more severe degree of softening and a wider softening area. But considering the fracture position (80% in the NZ, 20% along the TMAZ/NZ boundary) in this study, the softening in the HAZ did not dominate the fracture behaviour. The author attributed the abnormal fracture to tool features and the material flow pattern.

Esmaily et al. [25] acquired a high strength BT-FSW joint for 6005-T6 Al alloy, but the parameters are not totally consistent in the two processes, for which the parameter combination (rotation rate–welding speed) was 1200–100 for C-FSW and 900–1200 for BT-FSW. The parameter combination led to a faster cooling rate in BT-FSW than in C-FSW, so that a high strength BT-FSW joint was acquired.

Usually, 6000 series Al alloys in the T6 (artificial aging after solid solution heat-treatment) condition present a conventional FSW joint strength efficiency of 70–80% [41] and 60–80% for the T4 condition [43]. Esmaily et al. [25] and Lafly et al. [32] have reported that usually BT-FSW joints exhibit lower strength than that of C-FSW at corresponding parameters due to either the greater heat input or the flow pattern. In the present work, we obtained almost equivalent strength for BT-FSW joints compared with C-FSW joints at the same rotation rate and the same welding speed. We proved that the UTS and lowest hardness value in the HAZ are independent of the rotation rates but enhanced with increasing welding speed, which is in good agreement with Liu's and Zhang's experimental theory and modeling results [37,44]. The maximum UTS we obtained at C-600-300 reached 93% of the BM, and the BT-FSW BT-600-300 joint also reached 91% of the BM, which is competitive with the reported UTS of C-FSW joints being 60–80% of 6061-T4 Al alloy BM.

The tensile results can be demonstrated with the precipitates evolution in the HAZ. The increasing density and slight coarsening of  $\beta'$  (Fig. 6) compared with C-600-100 led to a relatively higher strength at BT-600-100. The phenomenon of the equivalent lowest hardness in the microhardness curves and UTS at different rotation rates in the two processes, and the rise of the lowest hardness and UTS at different welding speeds (Figs. 7 and 8) coincided well with the theory.

#### 3.4. Fracture Behaviour and Fractograph

For all the joints welded at various parameters, the tensile testing joints failed in the HAZ randomly at the advancing side or retreating side, except for samples of BT-600-300 which fractured along the NZ/TMAZ boundary, and typical macrographs showing the failure locations are presented in Fig. 9a–d. It can be seen that the deformation was mostly concentrated on one side for the C-FSW joints, which is different from the BT-FSW joints, where the deformation was located on both sides of the joints and fractured randomly on one side. It should be noted that, although a crack appeared along the NZ/TMAZ boundary during the tensile test of the BT-600-100 joint, the fracture behaviour was still dominated by the softening in the HAZ. The case of BT-600-300 is more severe, and caused some of the samples at parameter BT-600-300 to fracture along the NZ/TMAZ boundary. However, the transferring of the fracture position of the BT-600-300 sample did not have a devastating effect on the tensile properties. The formation of the hole on the AS could be attributed to the material flow considering the features of the pin.

For precipitation-hardened aluminium alloys (such as 2024, 6061 and 7075 from various series), it has been documented that HAZs are usually the LHZ due to the significant thermal cycles followed by dissolution/coarsening of the precipitates during FSW [42,44–48].

Fig. 10 shows the fractograph of the selected BT-600-100 and C-600-100 joints. It can be seen that the fracture surface was characterized by large dimples, showing a ductile fracture (Fig. 10b and d). At the bottom of the dimples, many precipitates were observed. It should be noted that the density of the precipitates in the BT-600-100 joint was higher than that of C-600-100 (Fig. 10b and d). This can be attributed to the slow cooling rate in BT-FSW. The exposure to higher temperature in the heat source (NZ) led to a slower cooling rate in the HAZ compared with C-FSW. The slower cooling rate allowed enough time for precipitation from the solid-solution matrix and coarsening, which was made clear from the TEM results (Fig. 6). The fractographs of the selected BT-600-300 joint are presented in Fig. 11. It can be seen that the BT-600-300 joint showed a V-pattern cavity feature (Fig. 11a) corresponding to Fig. 9c. However, it still presented a ductile fracture with large dimples (Fig. 11b). The observation of the V-pattern zone was also conducted (Fig. 11d, magnified C zone), and it also presented a ductile fracture with many small dimples. By contrast, the C-600-300 joint fractured with an inclination of a  $\sim 45^\circ$  angle to the weld centre (Fig. 12a), and it was also characterized by large dimples in the entire

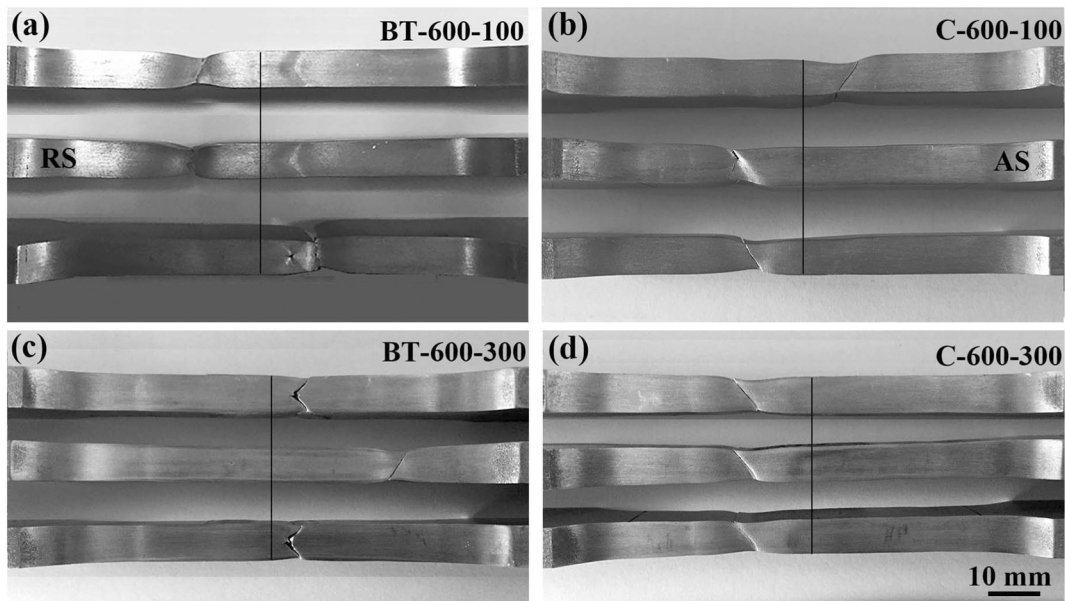


Fig. 9. Typical optical micrographs showing failure locations of 6061Al-T4 joints: (a) BT-600-100; (b) C-600-100; (c) BT-600-300; (d) C-600-300.

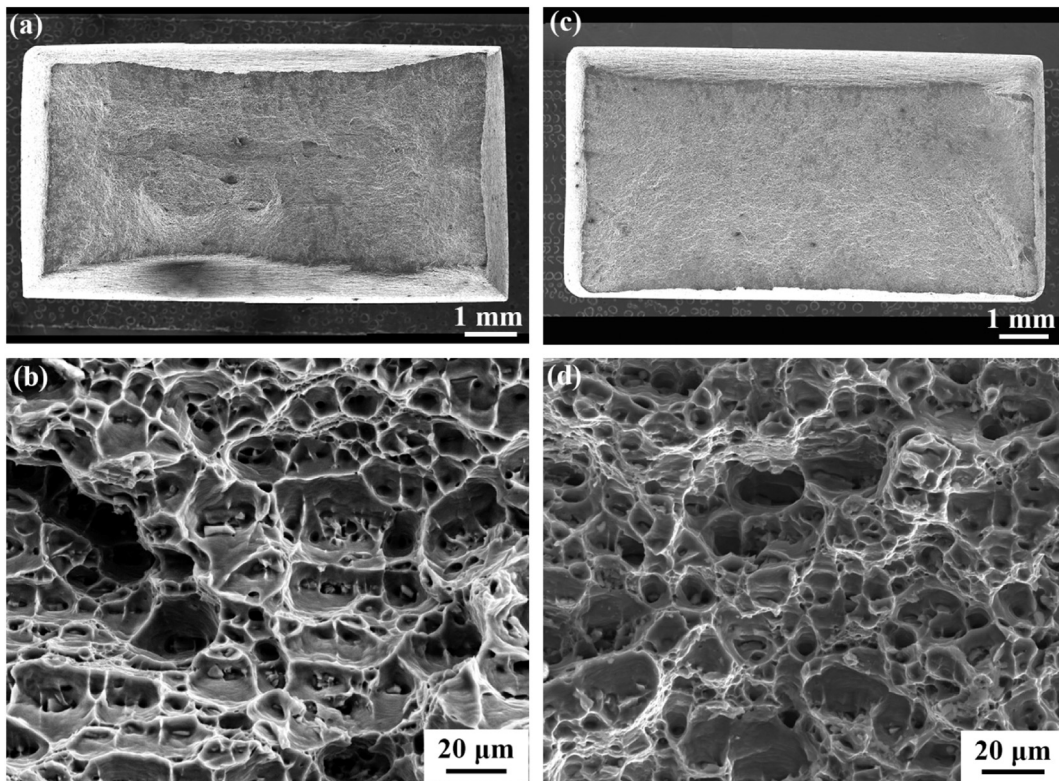


Fig. 10. Fractographs of 6061Al-T4 joints: (a), (b) for BT-600-100; (c) and (d) for C-600-100.

fracture surface (Fig. 12b).

#### 4. Conclusions

- (1) Defect-free joints of 6061-T4 Al alloy plates 6 mm in thickness were successfully welded by both BT-FSW and C-FSW processes but the BT-600-300 joint with BT-FSW has a narrower welding parameter window than that of C-FSW.
- (2) Both NZs in the two joints were characterized by fine equiaxed recrystallized grain structures with obvious joint line remnants in

the centres; in the HAZs,  $\beta'$  precipitates were apparently coarsened and the BT-FSW joints showed a higher density of  $\beta'$  precipitates than the C-FSW joints.

- (3) The hardness profiles exhibited a “W” shape along the centre line on the cross-section of both the joints, with the lowest hardness zone located in the HAZ; the lowest hardness remained at the same level for the two welding processes, independent of the rotation rate, and enhanced with increase of the welding speed; the hardness in the NZs increased slightly in the respective processes with increase of the welding speed, although this was not as evident when

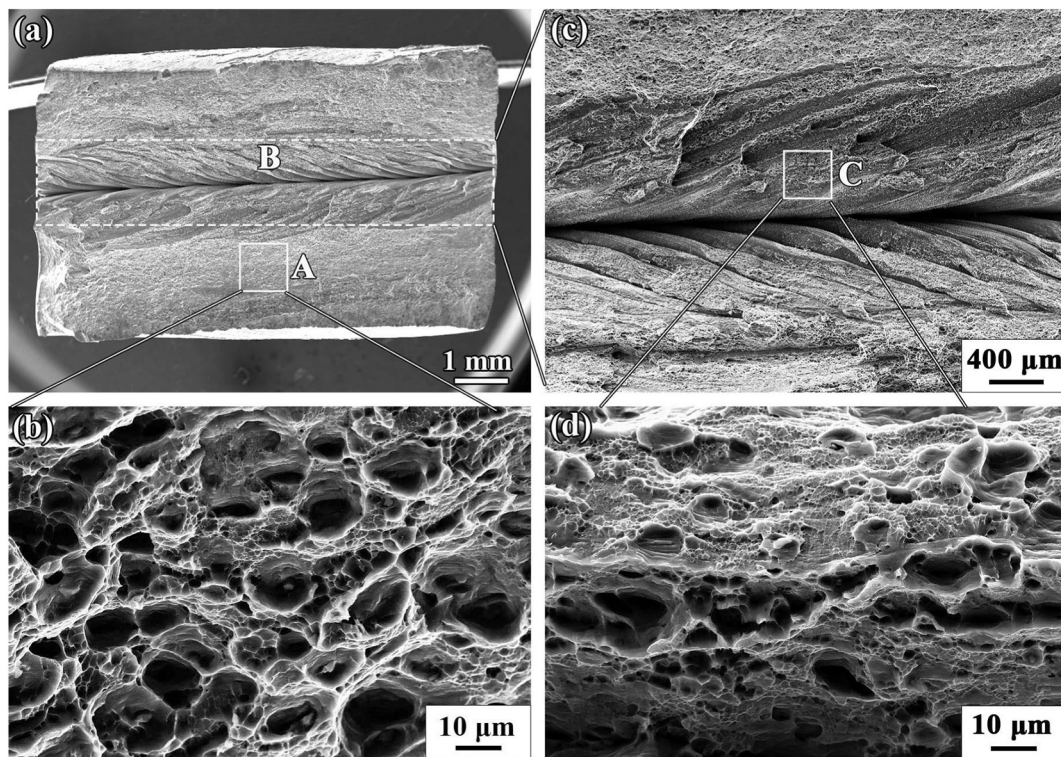


Fig. 11. Fractographs of BT-600-300 joint: (a) macro-fractograph, (b) magnified A zone; (c) magnified V-pattern zone (B zone) and (d) magnified C zone.

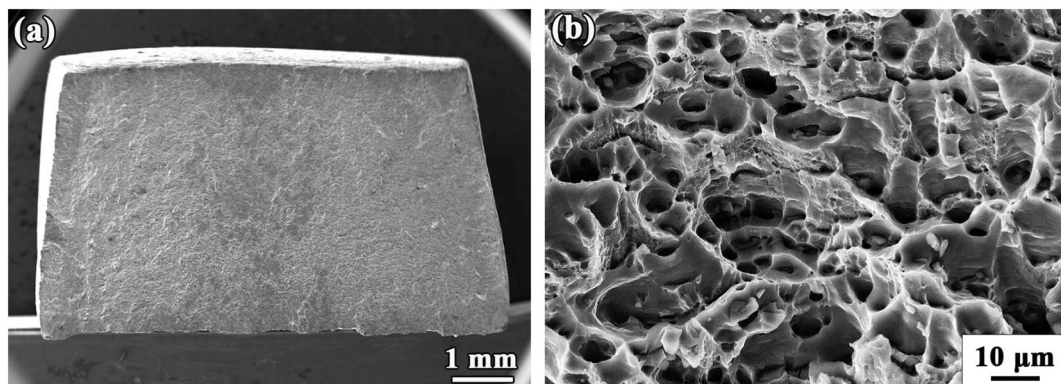


Fig. 12. Fractographs of C-600-300 joint: (a) macro-fractograph; (b) magnified microstructure in (a).

increasing the rotation rate.

- (4) The ultimate tensile strength was independent of the rotation rate and enhanced with increase of the welding speed. The maximum UTS (229 MPa) was achieved at the C-600-300 parameter, which was 93% of the base material.
- (5) The tensile joints mostly fractured in the HAZ, which is the lowest hardness zone. Typical fractographs showed a ductile fracture mode with large dimples on the fracture surface.

#### Acknowledgements

This work was supported by the National Natural Science Foundation of China under grant Nos. 51331008 and U1760201.

#### References

- [1] W.S. Miller, L. Zhuang, J. Bottema, A.J. Wittebrood, P. De Smet, A. Haszler, A. Vieregge, Recent development in aluminium alloys for the automotive industry, *Mater. Sci. Eng. A* 280 (1) (2000) 37–49.
- [2] M. Chen, X. Meng-Burany, T.A. Perry, A.T. Alpas, Micromechanisms and mechanics of ultra-mild wear in Al–Si alloys, *Acta Mater.* 56 (2008) 5605–5618.
- [3] R.S. Mishra, Z.Y. Ma, Friction stir welding and processing, *Mater. Sci. Eng. R* 50 (1–2) (2005) 1–78.
- [4] R.S. Mishra, De Partha Sarathi, N. Kumar, Friction Stir Welding and Processing, Springer International Publishing, Switzerland, 2014, pp. 1–338.
- [5] Y.Z. Li, Q.Z. Wang, B.L. Xiao, Z.Y. Ma, Effect of welding parameters and  $B_4C$  contents on the microstructure and mechanical properties of friction stir welded  $B_4C/6061Al$  joints, *J. Mater. Process. Technol.* 251 (2018) 305–316.
- [6] K. Zhao, Z.Y. Liu, B.L. Xiao, Z.Y. Ma, Friction stir welding of carbon nanotubes reinforced Al–Cu–Mg alloy composite plates, *J. Mater. Sci. Technol.* 33 (2017) 1004–1008.
- [7] D. Wang, B.L. Xiao, Q.Z. Wang, Z.Y. Ma, Evolution of the microstructure and strength in the nugget zone of friction stir welded  $SiCp/Al-Cu-Mg$  composite, *J. Mater. Sci. Technol.* 30 (2014) 54–60.
- [8] H. Shi, K. Chen, Z.Y. Liang, F.B. Dong, T.W. Yu, X.P. Dong, L.T. Zhang, A.D. Shan, Intermetallic compounds in the banded structure and their effect on mechanical properties of Al/Mg dissimilar friction stir welding joints, *J. Mater. Sci. Technol.* 33 (2017) 359–366.
- [9] P. Xue, D.R. Ni, D. Wang, B.L. Xiao, Z.Y. Ma, Effect of friction stir welding parameters on the microstructure and mechanical properties of the dissimilar Al–Cu joints, *Mater. Sci. Eng. A* 528 (2011) 4683–4689.
- [10] Wu L H, Nagatsuka K, Nakata K. Achieving superior mechanical properties in friction lap joints of copper to carbon-fiber-reinforced plastic by tool offsetting. *J. Mater. Sci. Technol.*, DOI: <https://doi.org/10.1016/j.jmst.2018.04.015>.
- [11] B.B. Wang, F.F. Chen, F. Liu, W.G. Wang, P. Xue, Z.Y. Ma, Enhanced mechanical

- properties of friction stir welded 5083Al-H19 joints with additional water cooling, *J. Mater. Sci. Technol.* 33 (2017) 1009–1014.
- [12] C. Rathinasuriyan, V.S. Senthil Kumar, Experimental investigation of weld characteristics on submerged friction stir welded 6061-T6 aluminum alloy, *J. Mater. Sci. Technol.* 31 (2017) 3925–3933.
- [13] S. Delrue, M. Tabatabaeipour, J. Hettler, K. Van Den Abeele, Applying a nonlinear, pitch-catch, ultrasonic technique for the detection of kissing bonds in friction stir welds, *Ultrasonics* 68 (2016) 71–79.
- [14] N.Z. Khan, A.N. Siddiquee, Z.A. Khan, S.K. Shihab, Investigations on tunneling and kissing bond defects in FSW joints for dissimilar aluminum alloys, *J. Alloys Compd.* 648 (2015) 360–367.
- [15] T. Le Jolu, T.F. Morgeneyer, A. Denquin, M. Sennour, A. Laurent, J. Besson, Microstructural characterization of internal welding defects and their effect on the tensile behavior of FSW joints of AA2198 Al-Cu-Li alloy, *Metall. Mater. Trans. A* 45 (2014) 5531–5544.
- [16] B.T. Gibson, D.H. Lammlein, T.J. Prater, W.R. Longhurst, C.D. Cox, M.C. Ballun, K.J. Dharmaraj, G.E. Cook, A.M. Strauss, Friction stir welding: process, automation, and control, *J. Manuf. Process.* 16 (2014) 56–73.
- [17] S.S. Chaudhary, K.H. Bhavsar, A review of bobbin tool friction stir welding, *Int. J. Sci. Technol. Eng.* 2 (10) (2016) 630–633.
- [18] J.C. Verduzco Juárez, G.M. Dominguez Almaraz, R. García Hernández, J.J. Villalón López, Effect of modified pin profile and process parameters on the friction stir welding of aluminum alloy 6061-T6, *Adv. Mater. Sci. Eng.* 2016 (2016) 1–9.
- [19] A.S. Sedmak, R. Kumar, S. Chattopadhyaya, S. Hloch, S.S. Tadic, A.A. Djurdjevic, I.R. Cekovic, E. Donceva, Heat input effect of friction stir welding on aluminium alloy AA 6061-T6 welded joint, *Therm. Sci.* 20 (2) (2016) 637–641.
- [20] S. Malopheyev, I. Vysotskiy, V. Kulitskiy, S. Mironov, R. Kaibyshev, Optimization of processing-microstructure-properties relationship in friction-stir welded 6061-T6 aluminum alloy, *Mater. Sci. Eng. A* 662 (2016) 136–143.
- [21] S.T. Selvamani, M. Vigneshwar, S. Divagar, Effects of heat transfer on microhardness and microstructure of friction stir welded AA 6061 aluminum alloy, *Int. J. Eng. Res. Afr.* 21 (2015) 102–109.
- [22] J. He, Z.M. Ling, H.M. Li, Effect of tool rotational speed on residual stress, microstructure, and tensile properties of friction stir welded 6061-T6 aluminum alloy thick plate, *Int. J. Adv. Manuf. Technol.* 84 (2015) 1953–1961.
- [23] H.I. Dawood, K.S. Mohammed, A. Rahmat, M.B. Uday, Effect of small tool pin profiles on microstructures and mechanical properties of 6061 aluminum alloy by friction stir welding, *Trans. Nonferrous Metals Soc. China* 25 (2015) 2856–2865.
- [24] A.H. Feng, D.L. Chen, Z.Y. Ma, Microstructure and low-cycle fatigue of a friction-stir-welded 6061 aluminum alloy, *Metall. Mater. Trans. A* 41 (2010) 2626–2641.
- [25] M. Esmaily, N. Mortazavi, W. Osikowicz, H. Hindsefelt, J.E. Svensson, M. Halvarsson, J. Martin, L.G. Johansson, Bobbin and conventional friction stir welding of thick extruded AA6005-T6 profiles, *Mater. Des.* 108 (2016) 114–125.
- [26] M. Esmaily, N. Mortazavi, W. Osikowicz, H. Hindsefelt, J.E. Svensson, M. Halvarsson, G.E. Thompson, L.G. Johansson, Corrosion behaviour of friction stir welded AA6005-T6 using a bobbin tool, *Corros. Sci.* 111 (2016) 98–109.
- [27] S.J. Chen, H. Li, S. Lu, R.Y. Ni, J.H. Dong, Temperature measurement and control of bobbin tool friction stir welding, *Int. J. Adv. Manuf. Technol.* 86 (2016) 337–346.
- [28] L. Wan, Y.X. Huang, Z.L. Lv, S.X. Lv, J.C. Feng, Effect of self-support friction stir welding on microstructure and microhardness of 6082-T6 aluminum alloy joint, *Mater. Des.* 55 (2014) 197–203.
- [29] M.K. Sued, D. Pons, J. Lavroff, E.H. Wong, Design features for bobbin friction stir welding tools: development of a conceptual model linking the underlying physics to the production process, *Mater. Des.* 54 (2014) 632–643.
- [30] Y. Morisada, T. Imaizumi, H. Fujii, Clarification of material flow and defect formation during friction stir welding, *Sci. Technol. Weld. Join.* 20 (2014) 130–137.
- [31] B. Li, Y.F. Shen, W.Y. Hu, The study on defects in aluminum 2219-T6 thick butt friction stir welds with the application of multiple non-destructive testing methods, *Mater. Des.* 32 (2011) 2073–2084.
- [32] A.L. Lafly, D. Allehaux, F. Marie, C.D. Donne, G. Biallas, Microstructure and Mechanical Properties of the Aluminium Alloy 6056 Welded by Friction Stir Welding Techniques, *50 Weld World*, 2006, pp. 98–106.
- [33] J. Zhang, G. Li, G.H. Luan, Comparison of Properties of Bobbin Tool FSW and Conventional FSWed 2219-T4 Al Alloy Joints, *Welding Technology in Aeronautics and Astronautics* 11 (2008), pp. 50–52.
- [34] M.W. Zandbergen, Q. Xu, A. Cerezo, G.D.W. Smith, Study of precipitation in Al-Mg-Si alloys by atom probe tomography I. Microstructural changes as a function of ageing temperature, *Acta Mater.* 101 (2015) 136–148.
- [35] F. Vahid, L. Brian, Nana Ofori-Opoku, R. Babak, P. Nikolas, E. Shahrzad, Cluster evolution mechanisms during aging in Al-Mg-Si alloys, *Acta Mater.* 103 (2016) 290–300.
- [36] S. Pogatscher A, H. Antrekowitsch, P.J. Uggowitzer, Interdependent effect of chemical composition and thermal history on artificial aging of AA6061, *Acta Mater.* 60 (2012) 5545–5554.
- [37] F.C. Liu, Z.Y. Ma, Influence of tool dimension and welding parameters on microstructure and mechanical properties of friction-stir-welded 6061-T651 aluminum alloy, *Metall. Mater. Trans. A* 39 (2008) 2378–2388.
- [38] N. Maruyama, R. Uemori, N. Hashimoto, M. Saga, M. Kikuchi, Effect of silicon addition on the composition and structure of fine-scale precipitates in Al-Mg-Si alloy, *Scr. Mater.* 36 (1997) 89–93.
- [39] I. Dutta, S.M. Allen, A calorimetric study of precipitation in commercial aluminum alloy 6061, *J. Mater. Sci. Lett.* 10 (1991) 323–326.
- [40] M. Peel, A. Steuwer, M. Preuss, P.J. Withers, Microstructure, mechanical properties and residual stresses as a function of welding speed in aluminum AA5083 friction stir welds, *Acta Mater.* 51 (2003) 4791–4801.
- [41] Y.S. Sato, H. Kokawa, M. Enomoto, S. Jogan, Microstructural evolution of 6063 aluminum during friction stir welding, *Metall. Mater. Trans. A* 30 (1999) 2429–2437.
- [42] D.R. Ni, D.L. Chen, D. Wang, B.L. Xiao, Z.Y. Ma, Influence of microstructural evolution on tensile properties of friction stir welded joint of rolled SiCp/AA2009-T351 sheet, *Mater. Des.* 51 (2013) 199–205.
- [43] D.M. Rodrigues, A. Loureiro, C. Leitao, R.M. Leal, B.M. Chaparro, P. Vilaca, Influence of friction stir welding parameters on the microstructural and mechanical properties of AA 6016-T4 thin welds, *Mater. Des.* 30 (2009) 1913–1921.
- [44] X.X. Zhang, B.L. Xiao, Z.Y. Ma, A transient thermal model for friction stir weld. Part II: effects of weld conditions, *Metall. Mater. Trans. A* 42 (2011) 3229–3239.
- [45] Z. Zhang, B.L. Xiao, Z.Y. Ma, Effect of welding parameters on microstructure and mechanical properties of friction stir welded 2219Al-T6 joints, *J. Mater. Sci.* 47 (2012) 4075–4085.
- [46] Z. Zhang, B.L. Xiao, Z.Y. Ma, Hardness recovery mechanism in the heat-affected zone during long-term natural aging and its influence on the mechanical properties and fracture behavior of friction stir welded 2024Al-T351 joints, *Acta Mater.* 73 (2014) 227–239.
- [47] Y.S. Sato, H. Kokawa, M. Enmoto, S. Jogan, T. Hashimoto, Microtexture in the friction-stir weld of an aluminum alloy, *Metall. Mater. Trans. A* 32 (2001) 941–948.
- [48] S.R. Ren, Z.Y. Ma, L.Q. Chen, Effect of welding parameters on tensile properties and fracture behavior of friction stir welded Al-Mg-Si alloy, *Scr. Mater.* 56 (2007) 69–72.